MNRAS **000**, 1–12 (2015) Preprint 27 October 2015 Compiled using MNRAS LaTeX style file v3.0

A Generic and Efficient E-field Parallel Imaging Correlator for Next-Generation Radio Telescopes

Nithyanandan Thyagarajan,[1]★ Adam P. Beardsley,[1] Judd D. Bowman[1] and Miguel F. Morales[2]
[1]*Arizona State University, School of Earth and Space Exploration, Tempe, AZ 85287, USA*
[2]*University of Washington, Department of Physics, Seattle, WA 98195, USA*

Accepted XXX. Received YYY; in original form ZZZ

ABSTRACT
Modern radio telescopes are favouring densely packed array layouts consisting of a large number of antennas ($N_\mathrm{a} \gtrsim 1000$–$\gtrsim 10000$). Since the complexity of traditional correlators scales as $\mathcal{O}(N_\mathrm{a}^2)$, there will be a steep cost for realizing the full imaging potential of these powerful instruments. Through our generic and efficient E-field Parallel Imaging Correlator (EPIC), we present the first software demonstration of a generalized direct imaging algorithm known as the Modular Optimal Frequency Fourier (MOFF) imager. It takes advantage of the multiplication-convolution theorem of Fourier transforms. Not only does it bring down the cost to $\mathcal{O}(N_\mathrm{a} \log N_\mathrm{a})$ but can also image from irregularly arranged heterogeneous antenna arrays. EPIC is highly modular and parallelizable. It is implemented in object oriented Python and is publicly available. We have verified the images produced to be mathematically identical to those produced using traditional techniques. We have also validated our implementation on data observed with the Long Wavelength Array. Antenna systems with a dense filling factor consisting of a large number of antennas such as LWA, SKA, and HERA will gain a significant advantage by deploying EPIC. Inherent availability of calibrated time-domain images on timescales roughly equal to the writeout timescale of the digitizer and vastly lower bandwidth relative to visibility based systems will make it a prime candidate for transient searches of Fast Radio Bursts (FRB) as well as planetary and exoplantenary phenomena.

Key words: instrumentation: interferometers – techniques: image processing – techniques: interferometric

1 INTRODUCTION

Radio astronomy is entering an era in which interferometers of hundreds to thousands of individual antennas are needed to achieve desired survey speeds. Nowhere is this more apparent than at radio frequencies below 1.4 GHz. The study of the history of hydrogen gas throughout the universe's evolution is pushing technology development towards arrays of low-cost antennas with large fields of view and densely packed apertures. Similarly, the search for transient objects and regular monitoring of the time-dependent sky is driving instruments in the same direction with the added requirement of fast read-outs. A number of new telescopes are under development around the world based on this new paradigm, including the Murchison Widefield Array (MWA;Tingay et al. 2013; Bowman et al. 2013), the Precision Array for Probing the Epoch of Reionization (PAPER; Parsons et al. 2010), the Hydrogen Epoch of Reionization Array[1] (HERA), the LOw Frequency ARray (LOFAR;van Haarlem et al. 2013), the Canadian Hydrogen Intensity Mapping Experiment (CHIME,Bandura et al. 2014), the Long Wavelength Array (LWA, Ellingson et al. 2013), and the low frequency component of the Square Kilometer Array Low Frequency Aperture Array (SKA1-Low Mellema et al. 2013).

This paradigm shift requires a fundamentally new approach to the design of digital correlators (Lonsdale et al. 2000). Modern correlators calculate the cross-power correlation between all antenna pairs in many narrow frequencies, forming *visibilities*, the traditional fundamental measurement of radio interferometers. The computational requirements for a modern FX correlator scale with the number of antenna pairs, or the square of the number of antennas $\sim N_\mathrm{a}^2$ (Bunton 2004). For this reason traditional correlators have difficulty scaling to thousands of antennas. As an example, the full HERA correlator for 352 dishes with 200 MHz of bandwidth requires 212 trillion complex multiplies and adds per second (TMACS). Future arrays with thousands of collecting elements will require orders of magnitude more computation, making the correlator the dominant cost.

For certain classes of radio arrays there is an alternative to the

★ E-mail: t_nithyanandan@asu.edu
[1] http://reionization.org

FX correlator that can lower the computational burden by directly performing a spatial fast Fourier transform (FFT) on the electric fields measured by each antenna in the array at each time step, removing the cross-correlation step. This relieves the computational scaling from the harsh N_a^2 to the more gentle envelope of $N_\mathrm{g}\log N_\mathrm{g}$, where N_g is the number of grid pixels in the Fourier transform (e.g. Morales 2011; Tegmark & Zaldarriaga 2009; Tegmark & Zaldarriaga 2010). This architecture is often referred to as a "direct imaging" correlator because it eliminates the intermediary cross-correlation data products of the FX and earlier lag correlators, but instead directly forms images from the electric field measurements.

Direct imaging correlators have begun to be explored on deployed arrays including the Basic Element for SKA Training II (BEST-2) array (Foster et al. 2014), the Omniscope (Zheng et al. 2014), and an earlier incarnation at higher frequencies with the intent of pulsar timing (Otobe et al. 1994; Daishido et al. 2000). However, each of these examples make assumptions about the redundancy of the array layout, and require the collecting elements are identical. On the other hand, the MOFF algorithm achieves the same $N_\mathrm{g}\log N_\mathrm{g}$ computational scaling without placing any restriction on antenna placement, can accommodate non-identical beam patterns, and is a provably optimal mapping (Morales 2011). This algorithm uses the antenna beam patterns to grid the electric field measurements to a regular grid in the software holography/A-transpose fashion (Morales & Matejek 2009; Bhatnagar, S. et al. 2008; Tegmark 1997a) before performing the spatial FFT. This process has been shown to theoretically produce a data product identical to images produced from the traditional FX correlator.

Here we present the first software implementation of the MOFF correlator, and announce the public release of the E-field Parallel Imaging Correlator (EPIC) code. We begin with a technical description of the algorithm in §2, then discuss our particular implementation in §3. We then verify the output data quality from our code in §4 by presenting simulated images from both the EPIC correlator and comparing to a simulated FX correlator. We also demonstrate the performance with real-world data from the LWA. In §5 we analyze the scaling relationships of the algorithm. We identify specific array design classes where the EPIC correlator is computationally more efficient and in the field of transients, demands significantly lesser bandwidth relative to visibility based approaches. We conclude and discuss future research prospects in §6.

2 MATHEMATICAL FRAMEWORK

We provide a brief summary of the mathematical equivalence of the MOFF and FX correlators detailed in Morales (2011). We first relate the dirty image produced from visibilities to the electric fields of astrophysical sources, then show that operations can be reordered to produce the same images at a lower computational cost.

Electric fields from astrophysical sources, $E(\hat{\mathbf{s}})$, in the sky coordinate system denoted by sine-projected unit vector $\hat{\mathbf{s}}$, propagate towards the observer as:

$$\widetilde{E}(\mathbf{r}) = \int E(\hat{\mathbf{s}})\, e^{-i2\pi\mathbf{r}\cdot\hat{\mathbf{s}}}\, \mathrm{d}^2\hat{\mathbf{s}}, \tag{1}$$

where, $\mathbf{r}$ denotes the observer's location (measured in wavelengths relative to some arbitrary origin) and $\widetilde{E}(\mathbf{r})$ is the propagated electric field. Thus the propagated electric field is a linear superposition of the electric fields emanating from astronomical sources with appropriate complex phases. It can also be described as a Fourier transform of the electric fields in the sky coordinates.

An antenna, a, measures a phased sum of these propagated electric fields over its effective collecting area with an additive receiver noise:

$$\begin{aligned}\widetilde{E}_a &= \int \widetilde{W}_a(\mathbf{r}-\mathbf{r}_a)\, \widetilde{E}(\mathbf{r})\, \mathrm{d}^2\mathbf{r} + \widetilde{n}_a &(2)\\ &= \int \widetilde{W}_a(\mathbf{r}-\mathbf{r}_a)\left[\int E(\hat{\mathbf{s}})\, e^{-i2\pi\mathbf{r}\cdot\hat{\mathbf{s}}}\, \mathrm{d}^2\hat{\mathbf{s}}\right]\mathrm{d}^2\mathbf{r} + \widetilde{n}_a &(3)\\ &= \int W_a(\hat{\mathbf{s}})\, E(\hat{\mathbf{s}})\, e^{-i2\pi\mathbf{r}_a\cdot\hat{\mathbf{s}}}\, \mathrm{d}^2\hat{\mathbf{s}} + \widetilde{n}_a &(4)\end{aligned}$$

where, $\widetilde{W}_a(\mathbf{r})$ is the aperture electric field illumination pattern of the antenna and its Fourier transform, $W_a(\hat{\mathbf{s}})$, is the directional antenna voltage response.

Interferometers measure *visibilities* – the degree of coherence between electric fields measured by a pair of antennas (van Cittert 1934; Zernike 1938; Thompson et al. 2001). A visibility, $\widetilde{V}_p$, can be written as:

$$\begin{aligned}\widetilde{V}_p &= \left\langle \widetilde{E}_a \widetilde{E}_b^\star \right\rangle_t &(5)\\ &= \Bigg\langle \left[\int W_a(\hat{\mathbf{s}})\, E(\hat{\mathbf{s}})\, e^{-i2\pi\mathbf{r}_a\cdot\hat{\mathbf{s}}}\, \mathrm{d}^2\hat{\mathbf{s}} + \widetilde{n}_a\right] \\ &\qquad \times \left[\int W_b^\star(\hat{\mathbf{s}}')\, E^\star(\hat{\mathbf{s}}')\, e^{i2\pi\mathbf{r}_b\cdot\hat{\mathbf{s}}'}\, \mathrm{d}^2\hat{\mathbf{s}}' + \widetilde{n}_b^\star\right]\Bigg\rangle_t &(6)\\ &= \iint W_a(\hat{\mathbf{s}})W_b^\star(\hat{\mathbf{s}}')\left\langle E(\hat{\mathbf{s}})E^\star(\hat{\mathbf{s}}')\right\rangle_t e^{-i2\pi(\mathbf{r}_a\cdot\hat{\mathbf{s}}-\mathbf{r}_b\cdot\hat{\mathbf{s}}')}\, \mathrm{d}^2\hat{\mathbf{s}}\, \mathrm{d}^2\hat{\mathbf{s}}', &(7)\end{aligned}$$

where we have brought the time average into the integral under the assumption that the aperture illumination pattern does not change over the time-scale of the averaging. This expression can be further simplified with the sky brightness, $I(\hat{\mathbf{s}}) = \left\langle E(\hat{\mathbf{s}})E^\star(\hat{\mathbf{s}}')\right\rangle_t \delta(\hat{\mathbf{s}}-\hat{\mathbf{s}}')$, and defining the antenna pair sky power response function (or the primary beam), $B_p(\hat{\mathbf{s}}) \equiv W_a(\hat{\mathbf{s}})\, W_b^\star(\hat{\mathbf{s}})$. The result is the visibility expressed in terms of the sky brightness, the primary beam, and uncorrelated noise terms which we group into $\widetilde{n}_p$,

$$\widetilde{V}_p = \int e^{-i2\pi\mathbf{u}_p\cdot\hat{\mathbf{s}}}\, B_p(\hat{\mathbf{s}})\, I(\hat{\mathbf{s}})\, \mathrm{d}^2\hat{\mathbf{s}} + \widetilde{n}_p, \tag{8}$$

where the baseline coordinate $\mathbf{u}_p = \mathbf{r}_a - \mathbf{r}_b$ is the vector separation between the two antennas. This signifies that the visibility ($\widetilde{V}_p$) measured between a pair of antennas (p) is obtained by the multiplying the sky brightness $I(\hat{\mathbf{s}})$ by the antenna power response $B_p(\hat{\mathbf{s}})$ and Fourier transforming from the directional coordinates ($\hat{\mathbf{s}}$) to uv coordinates, which are then sampled at the locations of the antenna spacings (or baselines), namely, $\mathbf{u}_p$, and added to the receiver noise n_p.

This can be equivalently re-written as:

$$\widetilde{V}_p = \int \tilde{B}(\mathbf{u}'-\mathbf{u}) \times \left[\int e^{-i2\pi\mathbf{u}.\hat{\mathbf{s}}}\, I(\hat{\mathbf{s}})\, \mathrm{d}^2\hat{\mathbf{s}}\right]\mathrm{d}^2\mathbf{u} + n_p, \tag{9}$$

where, $\tilde{B}(\mathbf{u})$ denotes the uv-space antenna power response obtained by a Fourier transform of $B(\hat{\mathbf{s}})$. Effectively, the multiplication in image space by $B(\hat{\mathbf{s}})$ has been replaced by a convolution with $\tilde{B}(\mathbf{u})$ in uv-space. This is the software holographic equivalent of traditional FX correlator output.

Hereafter, we adopt the matrix notation of Morales (2011), where vectors are represented with single coordinates, and matrices are represented by two coordinates denoting the spaces the operator transforms between. In this notation, the above measurement equation can be expressed as:

$$\mathbf{m}(\mathbf{v}) = \widetilde{\mathbf{B}}(\mathbf{v},\mathbf{u})\, \mathbf{F}(\mathbf{u},\hat{\mathbf{s}})\, \mathbf{I}(\hat{\mathbf{s}}) + \mathbf{n}(\mathbf{v}), \tag{10}$$

where the sky brightness $\mathbf{I}(\hat{\mathbf{s}})$ is Fourier transformed using $\mathbf{F}(\mathbf{u},\hat{\mathbf{s}})$

and the resultant spatial coherence function is weighted and summed using the antenna power response, $\widetilde{\mathbf{B}}(\mathbf{v},\mathbf{u})$ in uv-space sampled at the baseline location to obtain the measured visibilities:

$$\mathbf{m}(\mathbf{v}) = \left\langle \widetilde{\mathbf{E}}(\mathbf{a})\, \widetilde{\mathbf{E}}^{\star}(\mathbf{a}') \right\rangle_t , \tag{11}$$

where $\mathbf{m}(\mathbf{v})$ denotes visibilities measured by cross-correlating measured antenna electric fields over all possible pairs of $\mathbf{a}$ and $\mathbf{a}'$. It is the same as equation 5 written in matrix notation.

Using the optimal map-making formalism (Tegmark 1997b; Tegmark 1997a), a software holography image is formed using (Morales & Matejek 2009):

$$\mathbf{I}'(\hat{\mathbf{s}}) = \mathbf{F}^{\mathrm{T}}(\hat{\mathbf{s}},\mathbf{u})\, \widetilde{\mathbf{B}}^{\mathrm{T}}(\mathbf{u},\mathbf{v})\, \mathbf{N}^{-1}(\mathbf{v},\mathbf{v})\, \mathbf{m}(\mathbf{v}) \tag{12}$$

where the measured visibilities are weighted by the inverse of the system noise, followed by a gridding process using the holographic antenna power response as the gridding kernel, followed by a Fourier transform to create an image $\mathbf{I}'(\hat{\mathbf{s}})$. This is the optimal estimate of the true image $\mathbf{I}(\hat{\mathbf{s}})$ given the visibility measurements.

The intermediate step of gridding with the antenna power response can be expressed as a convolution of a data vector generated by gridding the electric fields directly with the antenna illumination pattern.

$$\widetilde{\mathbf{B}}^{\mathrm{T}}(\mathbf{u},\mathbf{v})\, \mathbf{N}^{-1}(\mathbf{v},\mathbf{v})\, \mathbf{m}(\mathbf{v}) = \\ \left\langle \left[\widetilde{\mathbf{W}}_a^{\mathrm{T}}(\mathbf{r},\mathbf{a})\, \widetilde{\mathbf{N}}^{-1}(\mathbf{a},\mathbf{a})\, \widetilde{\mathbf{E}}(\mathbf{a}) \right] * \left[\widetilde{\mathbf{W}}_a(\mathbf{r},\mathbf{a})\, \mathbf{N}^{-1}(\mathbf{a},\mathbf{a})\, \widetilde{\mathbf{E}}^{\star}(\mathbf{a}) \right] \right\rangle_t \tag{13}$$

We can then use the multiplication-convolution theorem to move the convolution in Equation 13 to a square after the Fourier transform in Equation 12.

$$\mathbf{I}'(\hat{\mathbf{s}}) = \left\langle \left| \mathbf{F}^{\mathrm{T}}(\hat{\mathbf{s}},\mathbf{r})\, \widetilde{\mathbf{W}}^{\mathrm{T}}(\mathbf{r},\mathbf{a})\, \widetilde{\mathbf{N}}^{-1}(\mathbf{a},\mathbf{a})\, \widetilde{\mathbf{E}}(\mathbf{a}) \right|^2 \right\rangle_t . \tag{14}$$

The term inside the angular brackets before squaring has a very similar form as that in equation 12. It signifies that the measured antenna electric fields are weighted by the antenna noise, weighted and gridded by the antenna aperture kernel, Fourier transformed and finally squared to obtain the same image estimated that would have been obtained using equation 12.

Equation 14 is the optimal imaging equation used by the MOFF algorithm. While mathematically equivalent to Equation 12, squaring in image space rather than convolving in uv space potentially saves orders of magnitude in computation.

There are some important differences between the two techniques:

(i) The time-averaging cannot be performed on a stochastic measurement but only on its statistical properties. In visibility based imaging, the visibilities measured between antenna pairs represent spatial correlations which can be time-averaged followed by gridding and imaging. However, in MOFF imaging both antenna and gridded electric fields are stochastic and therefore must be imaged and squared before time-averaging.

(ii) In visibility based imaging, electric fields measured by antennas are not correlated with themselves and hence lack zero spacing measurements. In contrast, in MOFF imaging, since the gridded electric fields are imaged and squared, they retain information from auto-correlated electric fields at zero spacing and thus yield the true total power of the imaged field.

3 SOFTWARE IMPLEMENTATION

We have implemented the MOFF imaging technique in our "E-field Parallel Imaging Correlator" – a highly parallelized Object Oriented Python package,[2] now publicly available. Besides implementing the MOFF imaging algorithm it also includes visibility based imaging using the software holography technique and a simulator for generating electric fields from a sky model.

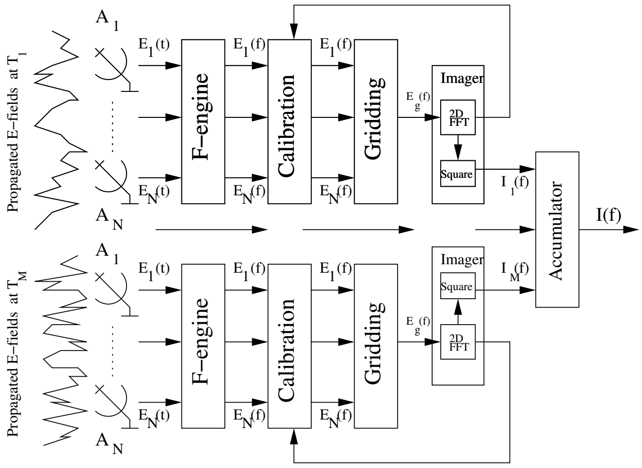

Figure 1. A flowchart of MOFF imaging in EPIC. The propagated electric fields shown on the left are measured as time-series $E_1(t)\ldots E_{\mathrm{N}}(t)$ by the antennas which are then Fourier transformed by the F-engine to produce electric field spectra $E_1(f)\ldots E_{\mathrm{N}}(f)$. They are calibrated and gridded. The gridded electric fields $E_{\mathrm{g}}(f)$ from each time series are imaged to produce an images $I_1(f)\ldots I_{\mathrm{N}}(f)$. These images are time-averaged to obtain the final image $I(f)$.

3.1 Data Flow

EPIC can accept dual-polarization inputs and produce images of all four cross-polarizations. Currently two data input formats exist for reading in the electric field time samples measured by the antennas – simulated electric fields based on a sky model using the simulator packaged with EPIC; and LWA data. Efforts to build interfaces for data from other telescopes are underway.

Fig. 1 shows the flowchart for MOFF imaging. The propagated electric fields are shown on the left at different time stamps, $t_1\ldots t_{\mathrm{M}}$. At each time stamp, the electric fields measured by antennas are denoted by $E_1(t)\ldots E_{\mathrm{N}}(t)$. The F-engine performs a temporal Fourier transform on the electric field time-series to obtain electric field spectra $E_1(f)\ldots E_{\mathrm{N}}(f)$ ($\widetilde{\mathbf{E}}(\mathbf{a})$ in matrix notation) for each of the antennas. Each of the complex antenna gains are calibrated to correct the corresponding electric field spectra. These calibrated electric fields are gridded using an antenna-based gridding convolution function after which it is spatially Fourier transformed and squared to obtain images for every time stamp. These images are then time-averaged to obtain the accumulated image $I(f)$ ($\mathbf{I}(\hat{\mathbf{s}})$ in matrix notation).

Fig. 2 shows the flowchart for a visibility based software holographic imaging from a FX correlator. The antenna-based F-engine is identical to that in the MOFF processing. The electric field spectra from each antenna are then cross-multiplied in the X-engine with those from all other antennas to obtain the visibilities $V_{\mathrm{ij}}(f)$ ($\mathbf{m}(\mathbf{v})$ in matrix notation). They are calibrated and time-averaged to obtain $\langle V_{\mathrm{ij}}(f)\rangle$ which are then gridded and imaged to obtain the

[2] EPIC package can be accessed at https://github.com/nithyanandan/EPIC

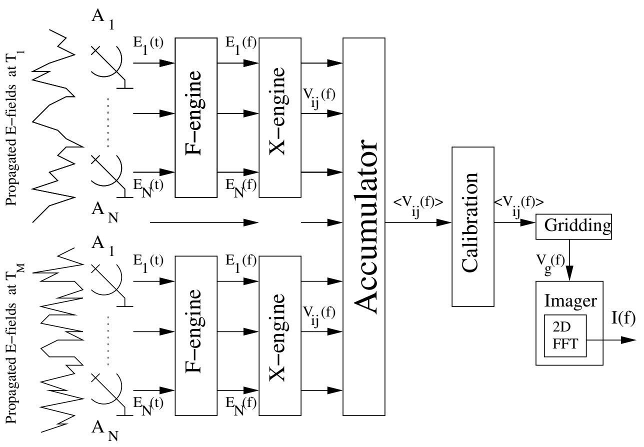

Figure 2. A flowchart of visibility based software holographic imaging in EPIC. The FX process flow shares the F-engine with the MOFF process. Following the F-engine, the electric fields pass through the X-engine to obtain visibilities $V_{ij}(f)$ which are calibrated and time-averaged. Then they are gridded to obtain the gridded visibilities $V_g(f)$ which are then Fourier transformed to obtain the image. $I(f)$.

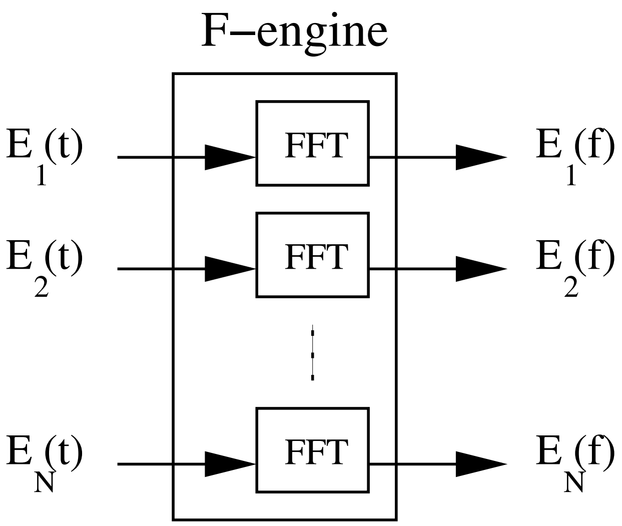

Figure 3. Block diagram of a F-engine. The electric field data streams from antennas are Fourier transformed in parallel to generate electric field spectra.

image $I(f)$. The $I(f)$ obtained from both techniques are identical as explained in §2.

Here we discuss the components of these architectures in detail.

Temporal Fourier transform

This module is common to the MOFF and visibility based imaging techniques. Time samples of electric fields measured by the antenna and digitized by the A/D converter is Fourier transformed to generate electric field spectra. This step can be parallelized by antennas as shown in Fig. 3. The output is then fed to either MOFF or visibility based imaging pipelines.

Antenna-to-Grid Mapping

A grid is generated on the coordinate system in which antenna locations are specified with a grid spacing. The grid spacing can be controlled by the user. By default, it is set to be at $\lambda_{\rm min}/2$ even at the highest frequency to ensure there is no aliasing even from regions of the sky far away from the field of view. The number of locations on the grid is restricted to be a power of 2.

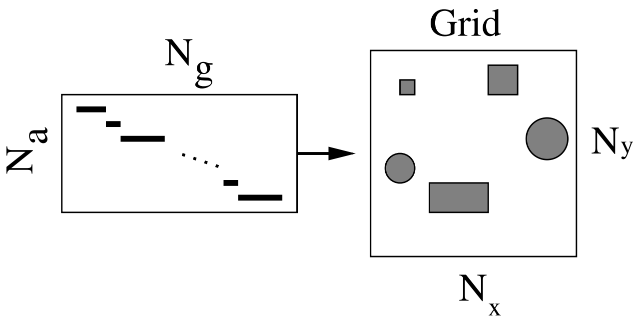

Figure 4. Block diagram of an antenna-to-grid mapping. A sparse block-diagonal matrix of total size $N_{\rm g} \times N_{\rm a}$ is created where each block contains roughly the number of pixels covered by the respective kernel. The antenna aperture illumination kernels do not have to be identical to each other. A discrete set of arbitrarily placed antennas are now placed onto a regular grid.

The gridding kernel in the simplest case is given by the antenna aperture illumination function, $\widetilde{B}(\mathbf{r}-\mathbf{r}_a)$, which can be specified either by a functional form or as a table of values against locations around the antennas. A nearest neighbor mapping from all antenna footprints to grid locations is created using an efficient k-d tree algorithm (Maneewongvatana & Mount 1999). There is no restriction here that the aperture illumination function has to be identical across antennas.

In the most general case, this gridding kernel could contain information on the w-projection effect, and even other time-dependent ionospheric effects. For a stationary antenna array in the absence of any time-dependent effects, this mapping must only be determined once in the antenna array coordinate frame. The antenna-to-grid mapping matrix, $\mathbf{M}(\mathbf{r},\mathbf{a})$ is described as a transformation matrix from the space of measured electric fields by the antennas ($\mathbf{a}$) to the antenna array grid denoted by the coordinate $\mathbf{r}$. Since each antenna occupies a footprint typically the size of its aperture, $\mathbf{M}(\mathbf{r},\mathbf{a})$, which is generally of size $N_{\rm g} \times N_{\rm a}$, reduces to a sparse block-diagonal matrix with only $N_{\rm a}$ blocks and roughly $N_{\rm k}$ non-zero entries per block. This sparse matrix is stored in a Compressed Sparse Row (CSR) format. Fig. 4 illustrates the antenna-to-grid mapping matrix and the grid containing the mapped aperture footprints of the antennas.

Calibration

Calibration of direct imaging correlators remains a challenge. Contrary to the FX data flow, direct imagers mix the signals from all antennas before averaging and writing to disk. It is therefore essential to apply gain solutions before the gridding step. Previous efforts have resorted to applying FX-generated calibration solutions (Zheng et al. 2014; Foster et al. 2014), or integrating a dedicated FX correlator which periodically forms the full visibility matrix (Wijnholds & van der Veen 2009; de Vos et al. 2009).

In a companion paper to appear soon, we demonstrate a novel calibration technique (EPICal) which leverages the data products formed by direct imaging correlators to estimate antenna complex gains. This method correlates the antenna electric field signals with an image pixel from the output of the correlator in the feedback calibration fashion outlined in Morales 2011 (illustrated in Fig. 1 by the arrow leading from the imager to the calibration block). Further-more it allows for arbitrarily complex sky models, and following the MOFF algorithm places no restriction on array layout, and accounts for non-identical antenna beam patterns. Because only a single correlation is needed for each antenna, the computation complexity scales only as $N_{\rm a}$.

The calibration module included in the EPIC repository allows for application of pre-determined calibration solutions, or can solve for the complex gains using the EPICal algorithm.

Gridding Convolution

The antenna array aperture illumination over the entire grid, $\widetilde{\mathbf{W}}(\mathbf{r})$, is obtained by a projection of the individual antenna aperture illuminations:

$$\widetilde{\mathbf{W}}(\mathbf{r}) = \sum_a \widetilde{\mathbf{W}}_a(\mathbf{r} - \mathbf{r}_a) \tag{15}$$

$$= \mathbf{M}(\mathbf{r},\mathbf{a})\, \mathcal{I}(\mathbf{a}), \tag{16}$$

where, $\mathcal{I}(\mathbf{a})$ is a row of ones. This is achieved by efficient multiplication with the sparse matrix created in the antenna-to-grid mapping process using the sparse matrices module in Python's SciPy package. Unless $\widetilde{\mathbf{W}}(\mathbf{r})$ includes time-dependent effects of the ionosphere or the instrument, it needs to be computed just once for the entire observation. However, the gridding of electric fields must be computed at every readout of the electric field spectra,

$$\widetilde{\mathbf{E}}(\mathbf{r}) = \mathbf{M}(\mathbf{r},\mathbf{a})\, \widetilde{\mathbf{E}}(\mathbf{a}). \tag{17}$$

Spatial Fourier Transform

Before the spatial Fourier transform, the gridded electric fields are padded with zeros in order to match the grid size and angular size of each image pixel that would have been obtained with software holography of output from an FX correlator.

In MOFF imaging, these are spatially Fourier transformed followed by a squaring operation at every timestamp for every frequency channel. In visibility based imaging, the spatial Fourier transform is performed only once per integration timescale and does not include a squaring operation.

Time-averaging

In MOFF imaging, the measured antenna electric fields and the corresponding holographic electric field images are zero-mean stochastic quantities. Hence, they cannot be time-averaged to reduce noise. The statistical quantity stable with time in this case are the square of the holographic electric field images. Thus, squared images have to be formed at every instant of time before averaging as indicated in equation 14.

In contrast, visibilities measured by an antenna are statistically stable within an integration time interval. Hence, they are averaged after calibration as shown in equation 5. It is advantageous to average them in visibilities before imaging because the repeated cost of spatial FFT can be avoided. Since this averaging has been performed already on the visibilities over an integration timescale, the imaging step has to be performed only once per integration cycle.

3.2 Software Architecture

EPIC is built using object oriented programming in Python and is built on carefully crafted modules which closely represent real-life entities in radio interferometer arrays and observations. The essential modules along with their key attributes and methods are illustrated in Fig. 5. These modules are described below.

3.2.1 Antenna Module

The antenna module is a fundamental building block upon which all the other modules are built. There is one antenna module per antenna each having attributes – the propagated electric field time-series, $E(t)$, and spectrum $E(f)$ for both polarizations. The most important function inside this module is the F-engine that Fourier transforms time-series electric field data into spectra.

The other function (not shown in the figure) is to update the data as new data keeps streaming in. This can also be parallelized. Another important attribute (not shown in figure) are antenna flags for each polarization appropriate for the data stream being held by the module.

3.2.2 Interferometer Module

The interferometer module holds the attributes and functions pertaining to a pair of antennas and represents the cross-correlation information obtained from the pair. Its primary attributes are the two antenna modules. It also contains four cross-polarized visibility time-series and spectra.

The critical component of the interferometer module is the X-engine. This is essentially a software analog of hardware correlators of real telescope systems. The X-engine can be toggled between two states of operation, namely, the FX and XF modes. The FX mode obtains the electric field spectra, $E(f)$ from the individual antenna modules inside this module and multiplies the two to obtain visibility spectra, $V(f)$. On the other hand, the XF mode cross-correlates the electric field time-series from its Antenna modules to obtain the visibilities as a function of lags, $V_t(t)$, which is then Fourier transformed to obtain $V(f)$. Both modules can operate on dual-polarizations to obtain all four cross-polarizations.

The other attributes (not shown in figure) are the flags applicable for each cross-polarization for the current data stream. Similar to the antenna module, it has an update function that can update the visibilities $V_t(t)$ or $V(f)$ directly rather than through the electric fields of its component antennas. This functionality is to allow EPIC to operate while attached to the backend of traditional correlator systems. This feature is not utilized for purposes of this paper.

This module forms the fundamental unit for the interferometer array module (to be discussed below) and in general for visibility based correlator and imaging systems.

3.2.3 Antenna Array Module

The antenna array module consists of all the antenna modules as its attributes and represents the collective properties of its component antennas. By virtue of holding each antenna data independently in their respective modules the F-engine for the entire array can be distributed to the F-engines of the component antenna modules thus achieving a highly parallelized F-engine while emulating real telescope systems.

The primary attributes held by this module are the antenna aperture illumination weights and electric fields projected on the grid using the gridding convolution method described above and implemented by the gridding function in this module. Significant parts of the antenna-to-grid mapping and gridding convolution are parallelizable across antennas and frequencies.

Individual antenna flags are carried over as additional weights to be applied to the gridded aperture illumination and electric fields. A series of data streams can be stacked up to take advantage of the

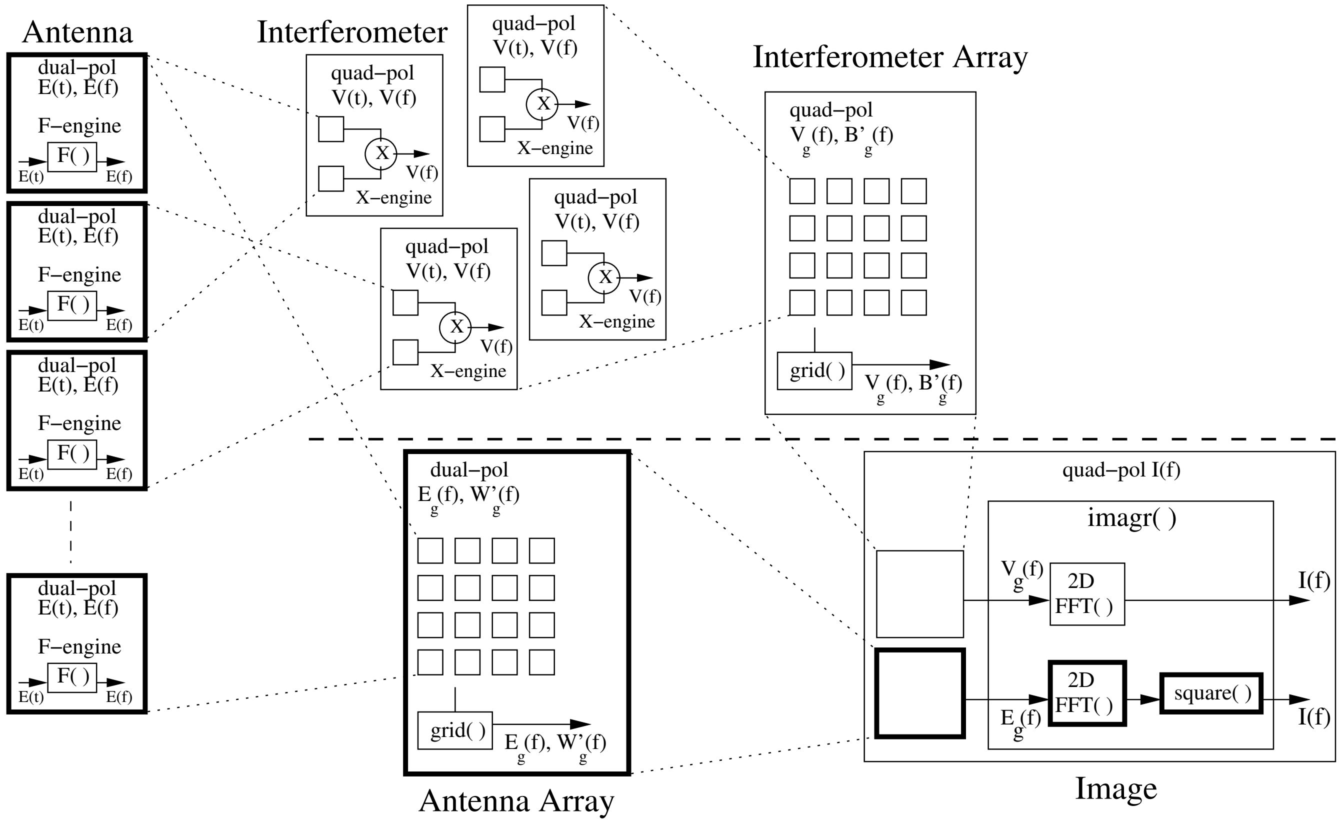

Figure 5. Software architecture of EPIC with core modules, their essential attributes and functions. The antenna module forms the fundamental building block. It consists of electric field time-series and spectra and the F-engine that performs a temporal FFT to obtain electric field spectra from the time-series. The interferometer module is made of a pair of antenna modules. Its main function is the X-engine (FX or XF) to produce visibility spectra. The antenna array module is made of all individual antenna modules as its components and contains collective properties about the antenna subsystems. Its core function is the creation of antenna-to-grid mapping and that of gridded aperture weights and electric fields. The interferometer array module is very similar in principle to the antenna array module except it operates on cross-correlations and produces gridded visibilities. The image module takes gridded electric fields or visibilities and performs a two-dimensional spatial FFT (and squares the intermediate image in case of the former) to produce output images. Broadly, the MOFF algorithm is implemented by modules below the horizontal dashed line while the visibility based imaging uses modules above the line. The exact processing pathway implementing the MOFF algorithm is shown in bolded modules.

array optimization available in Python. This module is also equipped to manage dual-polarization.

3.2.4 Interferometer Array Module

Similar to the antenna array module, the interferometer array module consists of individual interferometer modules. It can parallelize the correlator operations by distributing the X-operation over the X-engines of its component interferometer modules. The interferometer-to-grid mapping and gridding convolution are very similar in nature to that of the antenna array module. Flag-based grid weights, stacking and ability to handle all four cross-polarizations are built into this module.

3.2.5 Image Module

The image module is built as a general purpose module that can switch between operating on gridded electric fields or visibilities. At its heart, it consists of a two-dimensional spatial FFT where the padding can be specified by the user to control the resolution in the output images. In case of MOFF imaging, there is an additional step of squaring the holographic electric field images.

Besides its core functions of spatial Fourier transform and squaring, it can stack, accumulate and average images, and optionally remove the antenna auto-correlations centered around the zero-spacing pixel in the *uv* plane. It also handles all four cross-polarization products. Currently, it can support writing data out in standard FITS format.

4 VERIFICATION

In order to verify the accuracy of the EPIC code, we characterize the images produced through simulations. We simulate electric field streams from a model sky and process the data through both the MOFF and visibility based imaging algorithms. We then compare the output images to demonstrate their equivalence.

4.1 Simulations

We use the EPIC simulator to generate electric field samples from a sky model. In our simulations, we use 64 frequency channels each of width $\delta f = 40$ kHz, 10 point sources of flux densities 10 Jy at random locations. The number of timestamps integrated in one

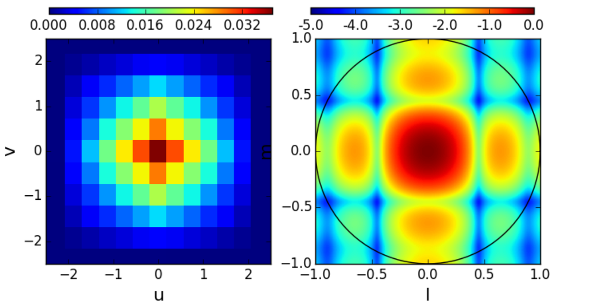

Figure 6. The auto-correlation of weights of a square shaped antenna aperture in the uv plane (left) and the corresponding directional antenna power response on the sky (right) in coordinates specified by direction cosines. The antenna auto-correlation weights are normalized to a sum of unity yielding a peak response of unity in the antenna's directional power pattern on the sky. The color scale for the directional power pattern is logarithmic. The black circle indicates the sky horizon and values beyond it are not physical and hence ignored.

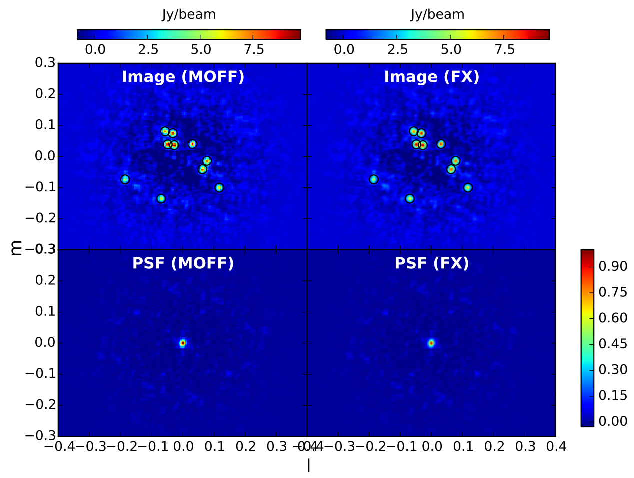

Figure 7. Dirty images (top) and synthesized beams (bottom) obtained from simulated data using antenna-based MOFF algorithm (left) and FX visibility-based software holography (right). The solid black circles in the top panels indicate the simulated source positions. The antenna auto-correlations at zero-spacing have been removed from the MOFF images. The images in either case reconstruct the sources at the right locations with the fluxes expected after multiplication by the antenna power pattern. The synthesized beams from the two algorithms are well matches in size and shape. The overall modulation by the power pattern is seen clearly in both images.

integration cycle was kept at eight where each A/D timeseries is $1/\delta f = 25\,\mu$s long. We use the MWA array layout (Beardsley et al. 2012) for demonstration. Only the inner 51 tiles within a square bounding box of 150 m on each side were used. We assumed all tiles are identical and have a square shaped electric field illumination footprint 4.4 m on each side.

4.2 Dealing with antenna auto-correlations

Before the outputs can be compared, we describe the elimination of a minor mathematical difference between the two techniques. The squaring operation under MOFF imaging in the image plane introduces antenna auto-correlations around the zero spacing in the uv-plane which are absent in traditional visibility based imaging. In order to facilitate a robust comparison between MOFF and visibility based imaging techniques, these auto-correlations are removed from both the MOFF algorithm output, which is otherwise not an essential part of the core algorithm. We describe below how they are removed.

The shape and extent of these auto-correlations can be estimated from the antenna aperture illumination pattern. The aperture illumination patterns are already available from the gridding step. Fig. 6 shows the estimated weights from antenna auto-correlations in the uv-plane (left) and the corresponding response in the image plane (right). The latter is simply the directional antenna power response.

We inverse Fourier transform the squared images and beams back to the uv plane and subtract the estimated auto-correlation kernel scaled to the peak value centered at the zero spacing pixel. The final averaged image is obtained by Fourier transforming the uv plane data and weights with the auto-correlations subtracted to the image plane. These images are now comparable to those obtained from visibility based imaging. This step of removing auto-correlations is optional and required to be performed only once per integration timescale and does not add significant cost to the full operation.

4.3 Comparison of outputs

We investigate the two imaging algorithms for differences from the point of view of the quality of their outputs. We begin by comparing the gridded cross-correlation weights in the uv-plane. In MOFF imaging, weights from antenna auto-correlations have been removed as described in §4.2.

Fig. 7 shows the dirty images (top) and synthesized beams (bottom) obtained with antenna-based MOFF and FX visibility based imaging algorithms packaged in EPIC. The antenna auto-correlations that correspond to zero spacing have been removed from the MOFF image and the corresponding synthesized beam. The sky positions of the simulated sources are indicated by solid black circles. The reconstructed sky image has the simulated sources at the expected sky positions in either case. Both algorithms result in images and synthesized beams that are well matched with each other. Their fluxes are modulated by a multiplicative power pattern corresponding to that of a uniform square aperture.

Fig. 8 shows the cross-correlation weights obtained with MOFF imaging (left) and visibility based imaging (right). The first notable difference is in the weights around zero spacing. Though both show a dominant void around zero-spacing, the void obtained with MOFF algorithm shows many pixels with non-zero weights. In contrast, the zero-spacing void from traditional imaging consists of predominantly zero-valued pixels. The gridding process in the former involves rounding the antenna footprint to the nearest grid pixel. Depending on the exact location of the center of the antenna relative to the grid, the grid pixels that receive contribution from an antenna may be a pixel narrower along one or both axes relative to that from another identical antenna but with a different center location relative to the grid. The resulting auto-correlation footprint will also not necessarily be identical. Hence, using a single expected footprint for subtraction will typically leave some residuals behind as seen in the void region in the weights obtained with MOFF imaging.

These residuals can be mitigated by:

(i) making the grid spacing finer which makes the rounding error

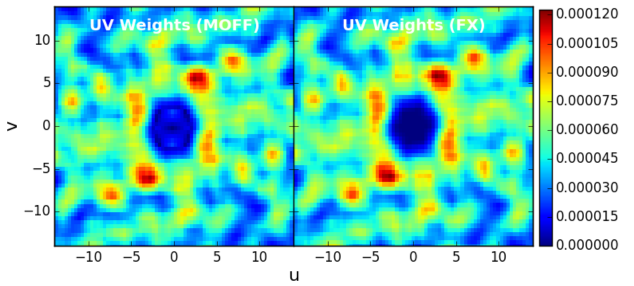

Figure 8. Dirty images (top) and synthesized beams (bottom) obtained from simulated data using antenna-based MOFF algorithm (left) and FX visibility-based software holography (right). The solid black circles in the top panels indicate the simulated source positions. The antenna auto-correlations at zero-spacing have been removed from the MOFF images. The images in either case reconstruct the sources at the right locations with the fluxes expected after multiplication by the antenna power pattern. The synthesized beams from the two algorithms are well matched in size and shape. The overall modulation by the power pattern is seen clearly in both images.

less susceptible to the location of the antenna center relative to the grid, and

(ii) subtracting each auto-correlation of antenna weights separately by using the shape and extent of the footprint appropriate for that specific antenna aperture.

The latter is the most general solution applicable especially in the case of heterogeneous antenna arrays and is under active development for EPIC.

The other notable difference is that weights outside the zero-spacing void in some regions are different from each other at the few percent level though the sum of weights in these regions are identical. For instance, note the difference in weights at $(u, v) \approx (2, -10)$. This is found to arise because with MOFF imaging the antenna locations were rounded to the nearest grid pixel whereas in visibility based imaging the baseline locations (difference between antenna locations) were rounded to the nearest grid pixel. Since rounding is not a commutative operation (i.e. rounding of the difference value is not necessarily equal to the difference of the rounded values), the gridding operation in the two cases introduces rounding errors in the placement of antenna aperture and cross-correlated aperture weights. Each antenna aperture weight projected to the nearest grid location can be displaced by $\sim$ 1–2 pixels. This effect can be mitigated only by making the grid spacing finer at the expense of increased computational cost.

We study the effect of the differences in gridded weights on the image plane. Fig. 9 shows the difference between the synthesized beams obtained with the two methods. A difference map between the two synthesized beams is shown on top. The amplitude of the difference appears to be modulated by the directional power response of the antenna. At the bottom, in radial bins, the rms of the synthesized beam (gray) and the rms of the difference map (black) are plotted in percentage units relative to the peak (to be read using the axis on the left side of the plot). The antenna power pattern (red; to be read using the scale on the right) is plotted for reference.

The synthesized beam rms is proportional to the antenna power pattern as expected from a point spread function uncorrected for the antenna power pattern. The rms of differenced synthesized beams is also modulated by the antenna power pattern. The rms of the difference is definitely lesser than the rms of the synthesized beam

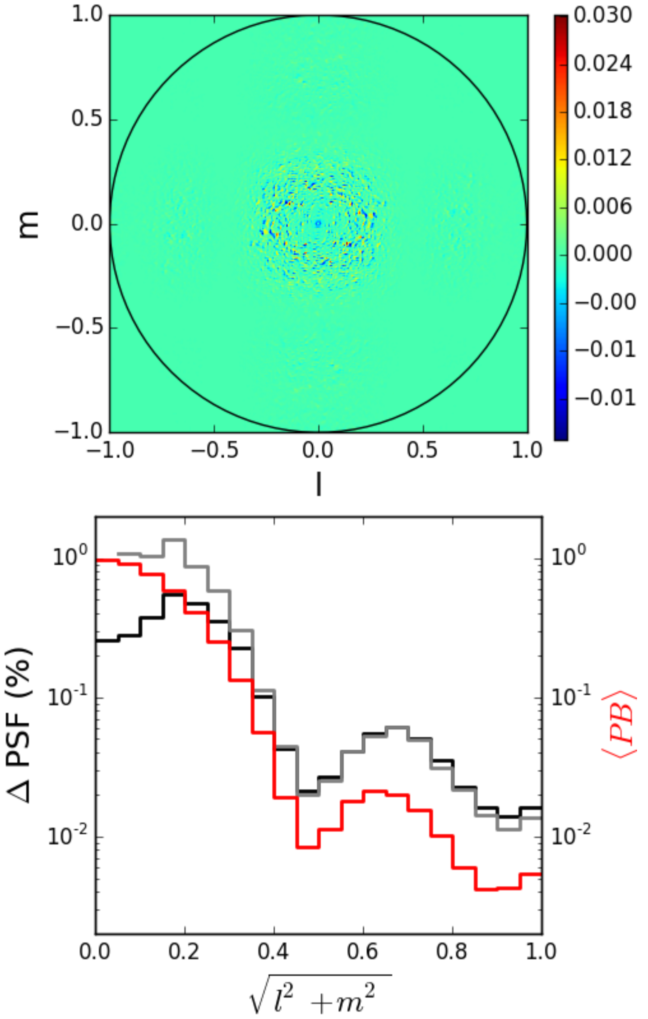

Figure 9. Map of difference between the synthesized beams obtained with the two methods (top) and radial statistics of the synthesized beams and their differences (bottom). The maximum difference is of the order of a few percent. The difference appears to be modulated in amplitude by the power pattern of the antenna.

in the central regions up to $(l^2 + m^2)^{1/2} \lesssim 0.3$. This implies that the beams are well matched in the central regions. In the outer regions, their mismatch is comparable to the rms of synthesized beams. This indicates the two synthesized beams are not completely randomly different from each other in which case the rms of the difference would have been $\approx \sqrt{2}$ higher than the rms of the each of the synthesized beams. This indicates that while differences exist, large fractions of them are still well matched to each other even out to the horizon. Thus the rounding errors in gridding do not affect the statistics of the images or the synthesized beams.

4.4 Application to LWA data

Here we demonstrate our software using narrow band data from the LWA in New Mexico. This data is in LWA narrow-band transient

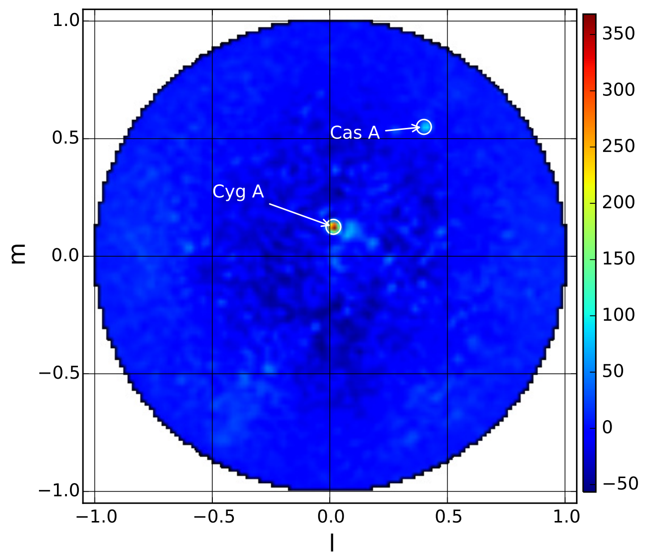

Figure 10. Image from LWA TBN data obtained with MOFF imaging using EPIC package after averaging over 2 s and ≈ 80 kHz. The x- and y-axes denote direction cosines l and m respectively. The antenna voltages are compensated for their respective delays. The flux scale is arbitrary and not calibrated. Locations of Cyg A and Cas A are annotated.

buffer (TBN) format with 512 voltage time samples from 255 antennas within roughly a diameter of 100 m. The data is centered at a frequency of 74.03 MHz, with a sample rate (equal to the bandwidth) of 100 kHz with 512 complex time samples in a A/D writeout timescale of 5.12 ms, a frequency resolution of 195.3125 Hz and dual polarization. There are 391 such timestamps yielding a total duration of 2 s.

We corrected the cable delays, but otherwise assume the data is sufficiently calibrated to image directly. A test of EPICal on this data will be conducted in the future.

Fig. 10 shows the image produced with MOFF imaging packaged in EPIC after averaging over the entire 2 s of data and the inner ≈ 80% of bandwidth (roughly 80 kHz). The image is shown in direction cosine coordinates – l along the horizontal axis and m along the vertical axis. The flux scale is arbitrary. Even in this proof-of-concept demonstration, we see Cyg A and Cas A prominently as annotated, thus validating the functionality of the EPIC package.

5 ANALYSIS AND FEASIBILITY

We now investigate the feasibility of implementing the EPIC imager on current and future radio telescopes.

5.1 Processing Volumes

We have profiled the core routines of EPIC line-by-line for various ranges of parameters such as antenna filling fraction, maximum baseline length, bandwidth and frequency resolution, integration timescale, etc. for HERA antenna layouts which are highly compact. However, we note that in general, the hardware and optimization of routines in place will determine the relative speeds of the different stages in the pipeline.

Of all steps in the MOFF pipeline that are repeated for every writeout from the F-engine, the slowest step even for dense HERA layouts is found to be the spatial two-dimensional FFT in the imaging stage relative to applying the sparse matrix gridding convolution, squaring or time-averaging. For instance, even in the dense array layout scenario that makes these stages perform the slowest, the gridding convolution, squaring and time-averaging take up only $\lesssim 20\%$, $\lesssim 20\%$ and $\lesssim 5\%$ respectively of the total time taken by all these processes while the spatial Fourier transform takes up $\gtrsim 55\%$ of the total time. With sparser arrays the gridding process will be be even faster.

In the visibility based imaging, the predominant computational cost is at the X-engine requiring $N_{\rm a}(N_{\rm a}-1)/2$ complex multiplications per channel at every correlator writeout timescale.

In the following discussions, we will assume that the computational cost for the MOFF imaging is determined by the spatial Fourier transform while that for visibility based imaging comes from $N_{\rm a}(N_{\rm a}-1)/2$ cross-correlations. However, if non-linearities such as non-coplanarity of baselines (Cornwell et al. 2008) and wide-field phenomena like the *pitchfork* effect (Thyagarajan et al. 2015a,b) are to be corrected for, the antenna based illumination footprint can start becoming less compact in the measurement plane and can result in a costlier gridding process.

The number of complex multiplications and additions in the spatial Fourier transform implemented via Fast Fourier Transform (FFT; Cooley & Tukey 1965) is $\approx \beta N_{\rm g} \log N_{\rm g}$ where $N_{\rm g}$ is the number of pixels on the grid and β is a constant that depends on the implementation of twiddle FFT algorithms (Brigham 1974). In our study, we set $\beta = 5$, a value[3] much more conservative than was indicated in Morales (2011). We set the number of complex multiplications in the X-engine in visibility based imaging to $N_{\rm a}^2$.

We consider a variety of current and planned radio telescopes. Their antenna layouts are summarized in Table 1. The size of the layout gives the maximum baseline $b_{\rm max}$. The grid spacing is determined by the science goals of the experiment in general. For our purpose, we assume a typical requirement that only the field of view of the antenna is to be imaged. This sets the grid spacing to be equal to the size of the antenna, $A_{\rm a}$. Hence, $N_{\rm g} \simeq b_{\rm max}^2/A_{\rm a}$.

Fig. 11 shows the number of complex operations per frequency channel per integration timescale. Telescopes that fall to the left of this line indicate MOFF imaging is computationally more efficient than visibility based imaging. All HERA layouts except possibly HERA-19 are in a parameter space where MOFF imaging holds the advantage. The solid line showing future trajectory of HERA like systems will be clearly favoured by MOFF imaging. The gray shaded area is for a projected LWA expansion and is also predominantly in the region favouring MOFF imaging. It is bounded by the LWA1 and LWA-OV on the left and right respectively. The current (see Table 1) and an expanded layout with a four-fold increase in number of elements over a 50% increase in $b_{\rm max}$ provide the bounds at the bottom and top respectively. Current instruments such as MWA and LOFAR lie in parameter space favouring visibility based imaging.

We now consider antenna array layouts described by three quantities essential to radio interferometry, namely, maximum baseline length, number of antennas, and the size of each antenna.

Fig. 12 shows the boundaries where the ratio of the number of computations required with visibility based imaging relative to

[3] http://www.fftw.org/speed/method.html

Table 1. Radio telescopes and array layouts.

Telescope	Core size $b_{\max}$ (in m)	Number of Antennas N_a	Antenna size A_a (in m^2)	Frequency f_0 (in MHz)
MWA-112[a]	1400	112	16	150
MWA-240[a]	1400	240	16	150
MWA-496[a]	1400	496	16	150
MWA-112[a]	1400	1008	16	150
LOFAR-LC[b]	3500	24	5809	50
LOFAR-HC[b]	3500	48	745	150
LWA1	100	256	10	50
LWA-OV[c]	200	256	10	50
HERA-19	70	19	154	150
HERA-37	98	37	154	150
HERA-331	294	331	154	150
HERA-6769[d]	1330	6769	154	150
SKA1-LC[e]	1000	750	962	150
SKA1-LCD[f]	1000	192,000	962	150
CHIME	100	1280	8	600
HIRAX	200	1024	6	600

[a] MWA-N denotes N tiles in the specified core diameter
[b] LC and HC denotes low band and high band stations inside the specified core diameter
[c] Owens Valley LWA
[d] Hypothetically chosen to have a total collecting area of 1 km^2
[e] This is the number of beamformed stations expected to be in the core, roughly three-fourths of the total number
[f] All dipoles inside the core are used as independent elements without station beamforming

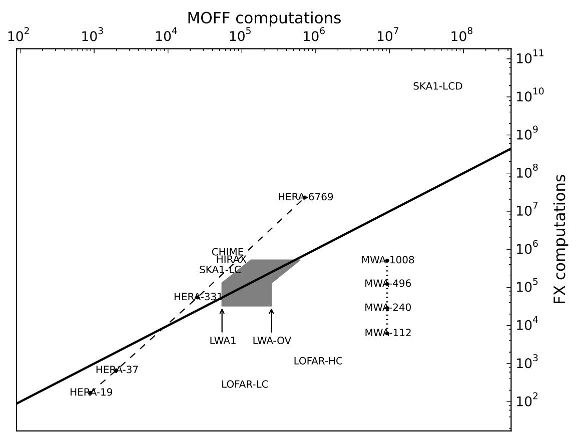

Figure 11. Current and planned instruments in parameter space of number of complex multiplies and adds with MOFF and FX. The dashed line is the boundary at which the number of operations with MOFF and visibility based imaging are equal. MOFF imaging is more efficient for telescopes occupying the left of this line and vice versa. CHIME, HIRAX and all the HERA layouts except HERA-19 and HERA-37 lie in the parameter space favoured by MOFF imaging. And so are SKA1-LC and SKA1-LCD. The solid black curve shows the projected trajectory of bigger close-packed hexagonal layouts similar to HERA. The gray shaded area denotes the projected trajectory of the LWA bounded by LWA1 (left edge), LWA-OV (right edge), current layout (bottom) and a four-fold increase in the number of elements within a 50% increase in the core size (top). Current instruments such as MWA and LOFAR fall in a region favoured by visibility based imaging.

MOFF imaging is unity. The different colored lines correspond to different antenna sizes (cyan - 1 m^2, blue - 7 m^2, purple - 16 m^2, green - 28 m^2, orange - 150 m^2, red - 740 m^2, gray - 5900 m^2). Solid line style in each color denotes the maximum number of antennas with the corresponding antenna size that can be densely packed inside various baseline lengths. The region to the right of the solid lines for corresponding antenna size represents a scenario of overlapping antennas that is physically impossible. Dashed lines of each color denote the boundary to the left of which visibility based imaging is favoured for the corresponding antenna size. Region inside the wedge enclosed by the solid and dashed lines favours using the MOFF algorithm for the corresponding antenna size over visibility based imaging. As antenna size increases the maximum number of antennas for a dense packing as a function of baseline length decreases. Hence, the solid lines shift leftward as antenna size increases. Similarly, with increase in antenna size, N_g also decreases when field of view imaging is achieved with an increasing grid spacing equal to antenna size and hence lowers the amount of computations required with the MOFF algorithm. This shifts the dashed curves leftward. The different antennas are color coded by roughly the class of antenna size they fall into. Thus symbols of one color falling into a wedge of the same color indicates MOFF imaging is favoured for those telescopes and vice versa. For e.g., MOFF imaging is favoured in HERA-33 and HERA-6769 because they are inside the wedge but not so in cases of HERA-19 and HERA-37. A majority of the next-generation radio telescopes, namely, HERA-331 and its future expanded versions, SKA1-LC, SKA1-LCD, HIRAX, CHIME, LWA1 and its future expansions (LWA1-x2x1 and LWA1-x4x1.5 denote two-fold and four-fold increase in the number of antennas within a core diameter that is 1 and 1.5 times the current size of 100 m respectively), and a couple of the expanded versions of LWA-OV (LWA-OVx2x1 and LWA-OVx4x1.5 denote two-fold and four-fold increase in the number of antennas within a core diameter that is 1 and 1.5 times the current size of 200 m respectively) will fall in the regime where MOFF imaging will be desirable. For a fixed baseline length, regions favouring the MOFF algorithm tend to be towards large N_a indicating large-N dense array layouts with smaller antenna elements are best suited for deploying EPIC.

5.2 Data Throughput

We elaborate on the data rates required with the MOFF and visibility based algorithms. This is particularly relevant in the context of radio transient detection pipelines.

Implementation of the MOFF algorithm with EPIC yields calibrated images on timescales of the output generated by the digitizer and is set by the inverse of the frequency channel width. These calibrated images are accumulated and averaged to a certain timescale depending on science or hardware requirements, or when the sky has rotated significantly, whichever is lesser. In visibility based algorithms, the visibilities are accumulated and averaged to this timescale before images are produced. Thus the data throughput (in samples per second) with MOFF and X-engine outputs are:

$$r_{\mathrm{MOFF}} \sim \frac{4N_g}{\Delta t}\left(\frac{\Delta B}{\Delta f}\right) \tag{18}$$

$$r_X \sim 2\,\frac{N_a(N_a-1)/2}{\Delta t}\left(\frac{\Delta B}{\Delta f}\right), \tag{19}$$

where, factor 4 in the expression for r_{MOFF} accounts for imaging after zero-padding the gridded electric fields, the leading factor

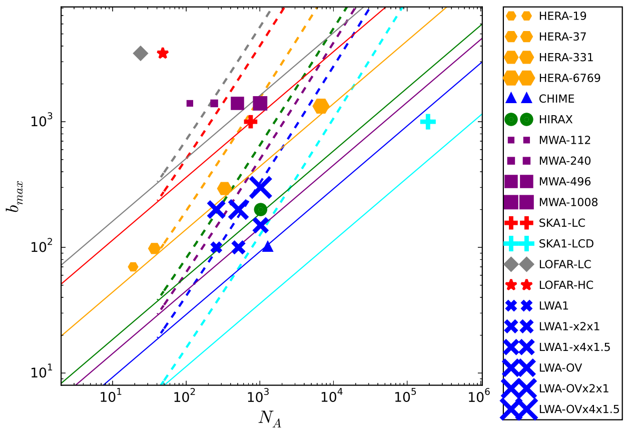

Figure 12. Current and planned instruments in parameter space of baseline length and number of antennas with MOFF and FX. Line styles of different colors denote different classes of antenna sizes (cyan - 1 m^2, blue - 7 m^2, purple - 16 m^2, green - 28 m^2, orange - 150 m^2, red - 740 m^2, gray - 5900 m^2). Solid line style in each color denotes the maximum number of antennas with the corresponding antenna size that can be packed inside various baseline lengths. The region to the right of the solid lines for corresponding antenna size is physically disallowed. Dashed lines of each color denote the boundary to the left of which visibility based imaging is favoured for the corresponding antenna size. Region inside the wedge enclosed by the solid and dashed lines favours using the MOFF algorithm for the corresponding antenna size. These wedges shift leftward with increasing antenna size. The different antennas are color coded by roughly the class of antenna size they fall into. Thus symbols of one color falling into a wedge of the same color indicates MOFF imaging is advantageous for those telescopes and vice versa. For e.g., MOFF imaging is favoured in HERA-33 and HERA-6769 because they are inside the wedge but not so in cases of HERA-19 and HERA-37.

of 2 in the expression for $r_{\rm X}$ accounts for the real and imaginary parts of the complex visibilities, ΔB is the bandwidth, Δf is the frequency resolution, and Δt is the timescale over which the transient phenomenon is sampled and the data (images or visibilities) are averaged to.

Though a full understanding of the FRB phenomena is yet to emerge, there are indications the timescales of FRB objects are $\Delta t \sim 1$–10 ms (Thornton et al. 2013). For a telescope like HERA, $\Delta B \simeq 100$ MHz, $\Delta f \simeq 100$ kHz. For HERA-331, $N_{\rm a} = 331$ and with a grid spacing to image the field of view, $N_{\rm g} \simeq 441$ or $N_{\rm g} \simeq 1024$ if $N_{\rm g}$ is preferred as a power of 2. Using 8 bytes for each floating point sample, the throughputs are $r_{\rm MOFF} \lesssim 3$ GB/s and $t_{\rm X} \simeq 81$ GB/s. For HERA-37, $r_{\rm MOFF} \lesssim 190$ MB/s and $t_{\rm X} \simeq 1$ GB/s. In such a case, The X-engine throughput corresponds to $\simeq 3.5$ TB an hour. Conversely, for the same data throughput, the MOFF algorithm can sample even shorter timescales. Table 2 shows these data rates for some of the current and planned telescopes for $\Delta t = 10$ ms.

Thus even with conservative estimates, the MOFF algorithm provides very economic data throughput for a majority of next generation radio telescopes with a dense layout. The most significant advantage is that calibrated images are also available at no extra cost.

Table 2. Data throughput for various telescopes with MOFF and X-engine outputs on timescales of $\Delta t = 10$ ms assuming $\Delta B = 100$ MHz and $\Delta f = 100$ kHz.

Telescope[a]	$r_{\rm MOFF}$[b] (GB/s)	$r_{\rm X}$ (GB/s)
LWA1	$\simeq 3$	$\simeq 48.5$
LWA-OV	$\simeq 12$	$\simeq 48.5$
HERA-19	$\lesssim 0.19$	$\simeq 0.25$
HERA-37	$\lesssim 0.19$	$\simeq 1$
HERA-331	$\lesssim 3$	$\simeq 81$
CHIME	$\lesssim 6.1$	$\simeq 1220$

[a] Antenna layouts are listed in Table 1.
[b] $N_{\rm g}$ is usually greater than true value because of rounding to the next power of 2. Thus $r_{\rm MOFF}$ estimates are usually lesser than the conservative values listed here.

6 CONCLUSIONS

As radio astronomy is entering a new era, advances in instrumentation have to be accompanied by equal advances in processing techniques to manage computational resources. Many future radio telescopes such as the SKA, HERA and LWA are headed towards the large-N dense array layout model for which computational cost from traditional FX/XF correlator based architecture and visibility based imaging starts rising steeply. We have provided the first software demonstration of a general purpose imaging algorithm using our generic and efficient EPIC software that is designed to bring this cost down from $O(N^2)$ to $O(N \log N)$. Under the class of direct imaging techniques, ours is one of the most generic – neither does it place any constraint on the array layout to be on a regular grid nor does it require the antenna array to be homogeneous.

Our package, now publicly available, written in object oriented Python is highly modularized and parallelizable. It includes an implementation of the MOFF algorithm in addition to visibility based software holography imaging and a data simulator for sky models. It has been successfully tested on simulated as well as real LWA observations.

The MOFF algorithm packaged with EPIC is already found to be most suitable for many present and planned radio telescopes such as the LWA, HERA and SKA. In general, MOFF is most suited to operate in the region of parameter space characterized by dense packing of a large number of antennas especially when consisting of a large number of small antenna elements.

A unique advantage is the instantaneous availability of calibrated time-domain images bundled together with the hardware frontend such as the F-engine as an integrated module with significant savings in data throughput relative to a X-engine based pipeline. Hence, it is a compelling candidate for time-domain radio astronomy, e.g. search for and monitoring of transients. Transient detection pipeline at the backend of EPIC can be fine-tuned to target fast transients such as the Fast Radio Bursts (FRB; Thornton et al. 2013) on millisecond timescales at GHz frequencies or slow transients from planetary and exoplanetary origins at frequencies around 100 MHz.

Thus, EPIC with the MOFF algorithm packaged is uniquely poised to offer a substantial advantage to imaging with large-N dense arrays typical of next-generation radio telescopes as well as push the frontiers of time-domain astronomy to fill gaps in understanding the science behind phenomena responsible for extreme transient events in the Universe.

In the near future, we plan to upgrade our current Python implementation of EPIC to a GPU based pipeline in order to operate on real-time data and develop a transient trigger and monitor backend. In the meanwhile, we plan to demonstrate the capability of EPIC to calibrate and image from heterogeneous arrays and incorporate corrections for non-coplanarity of baselines and direction-dependence of calibration.

ACKNOWLEDGEMENTS

We thank Greg Taylor for providing us the LWA data, and Larry D'Addario, Gregg Hallinan and Harish Vedantham for their valuable inputs. Construction of the LWA has been supported by the Office of Naval Research under Contract N00014-07-C-0147. Support for operations and continuing development of the LWA1 is provided by the National Science Foundation under grant AST-1139974 of the University Radio Observatory program.

REFERENCES

Bandura K., et al., 2014, in Society of Photo-Optical Instrumentation Engineers (SPIE) Conference Series. p. 22 (arXiv:1406.2288), doi:10.1117/12.2054950
Beardsley A. P., et al., 2012, MNRAS, 425, 1781
Bhatnagar, S. Cornwell, T. J. Golap, K. Uson, J. M. 2008, A&A, 487, 419
Bowman J. D., et al., 2013, Publ. Astron. Soc. Australia, 30, 31
Brigham E. O., 1974, The fast Fourier Transform
Bunton J. D., 2004, Experimental Astronomy, 17, 251
Cooley J. W., Tukey J. W., 1965, Math. Comput., 19, 297
Cornwell T. J., Golap K., Bhatnagar S., 2008, IEEE Journal of Selected Topics in Signal Processing, 2, 647
Daishido T., et al., 2000, Proc. SPIE, 4015, 73
Ellingson S. W., et al., 2013, IEEE Transactions on Antennas and Propagation, 61, 2540
Foster G., Hickish J., Magro A., Price D., Zarb Adami K., 2014, Monthly Notices of the Royal Astronomical Society, 439, 3180
Lonsdale C. J., Doeleman S. S., Cappallo R. J., Hewitt J. N., Whitney A. R., 2000, in Butcher H. R., ed., Society of Photo-Optical Instrumentation Engineers (SPIE) Conference Series Vol. 4015, Radio Telescopes. pp 126–134
Maneewongvatana S., Mount D. M., 1999, eprint arXiv:cs/9901013,
Mellema G., et al., 2013, Experimental Astronomy, 36, 235
Morales M. F., 2011, PASP, 123, 1265
Morales M. F., Matejek M., 2009, MNRAS, 400, 1814
Otobe E., et al., 1994, PASJ, 46, 503
Parsons A. R., et al., 2010, The Astronomical Journal, 139, 1468
Tegmark M., 1997a, Phys. Rev. D, 55, 5895
Tegmark M., 1997b, ApJ, 480, L87
Tegmark M., Zaldarriaga M., 2009, Phys. Rev. D, 79, 083530
Tegmark M., Zaldarriaga M., 2010, Phys. Rev. D, 82, 103501
Thompson A. R., Moran J. M., Swenson Jr. G. W., 2001, Interferometry and Synthesis in Radio Astronomy, 2nd Edition. Wiley
Thornton D., et al., 2013, Science, 341, 53
Thyagarajan N., et al., 2015a, ApJ, 804, 14
Thyagarajan N., et al., 2015b, ApJ, 807, L28
Tingay S. J., et al., 2013, PASA - Publications of the Astronomical Society of Australia, 30
Wijnholds S., van der Veen A.-J., 2009, Signal Processing, IEEE Transactions on, 57, 3512
Zernike F., 1938, Physica, 5, 785
Zheng H., et al., 2014, MNRAS, 445, 1084
de Vos M., Gunst A., Nijboer R., 2009, Proceedings of the IEEE, 97, 1431
van Cittert P. H., 1934, Physica, 1, 201
van Haarlem M. P., et al., 2013, A&A, 556, A2

This paper has been typeset from a TeX/LaTeX file prepared by the author.